Available online at www.sciencedirect.com

ScienceDirect

Procedia CIRP 58 (2017) 549 – 554

www.elsevier.com/locate/procedia

16th CIRP Conference on Modelling of Machining Operations

Cutting simulations of two gear steels with microstructure dependent material laws

Mustapha Abouridouane[a,*], Gottfried Laschet[b], Viktor Kripak[c], Andre Texeira[a], Jens Dierdorf[d], Ulrich Prahl[c], Fritz Klocke[a]

[a]*Laboratory for Machine Tools and Production Engineering (WZL), RWTH Aachen University*
[b]*ACCESS e.V., RWTH Aachen University, Germany*
[c]*Department of Ferrous Metallurgy (IEHK), RWTH Aachen University, Germany*
[d]*Institute of Metal Forming (IBF), RWTH Aachen University, Germany*

* Corresponding author. Tel.: +49-241-8028176; fax: +49-241-8022293. *E-mail address:* m.abouridouane@wzl.rwth-aachen.de.

Abstract

Within this work, a multiscale approach is presented investigating the effect of the ferrite-pearlite microstructure after annealing on the subsequent machining process of a steel gear. The case-hardening steel 18CrNiMo7-6 and a cost efficient alternative with reduced Cr and Ni content have been studied. Based on an advanced microstructure characterization an effective Johnson-Cook hardening law is derived for both steel grades via homogenization and is used in subsequent orthogonal cutting simulations based on the Coupled Eulerian-Lagrange approach. Machinability predictions are validated by comparing with cutting experiments proving the adopted multiscale approach.

Peer-review under responsibility of the scientific committee of The 16th CIRP Conference on Modelling of Machining Operations

Keywords: Orthogonal Cutting; Microstructure Characterization; Multiscale Modelling; Homogenization; Johnson-Cook Material Law.

1. Introduction

Hot-forged steel gear wheels are widely used e.g. in wind energy converters. Their manufacturing process chain involves various process steps such as continuous casting, hot rod rolling and forging, followed by a direct annealing to produce a ferrite-pearlite microstructure suitable for machining the gear preform.

In this study, two different steel grades are retained to manufacture gear preforms: the reference 18CrNiMo7-6 alloy, commonly used in automotive gears, and a lower cost variant. Indeed, in order to reduce the production costs and increase its performance, a variant, named “substitute”, has been developed recently by removing the expensive Ni, reducing Cr and adding Mn and Mo [1]. In order to investigate the impact of their chemistry and ferrite-pearlite microstructure after annealing on the subsequent cutting process step, predictive micro-models have to be established and integrated into a comprehensive virtual simulation platform [2]. Such platform allows the consideration of all relevant phenomena at the micro-scale within the macro-simulations of the gear production.

As extreme conditions (high strain rates, elevated temperatures) occur during the cutting process, specific effective material laws of the steel grades have to be derived for the orthogonal cutting simulation. One of the common models is the Johnson-Cook (JC) model [3], in which the strain hardening, the strain rate and temperature dependent material parameters are determined by fitting experimental dynamic flow curves at various strain rates and temperatures. These constants do not include microstructure dependent parameters such as grain size, phases and dislocation densities, although they influence the material dynamic response [4-5].

Thus, in the present study, the aim is to derive microstructure dependent hardening parameters of the JC model. To achieve this goal, material models have to be specified for each involved phase at the microscale. Experimental characterization of both

Peer-review under responsibility of the scientific committee of The 16th CIRP Conference on Modelling of Machining Operations
doi:10.1016/j.procir.2017.03.332

steel grades, outlined in section 2, determines their microstructural features (grain size, the interlamellar spacing, pearlite content) and identifies the nature and shape of the inclusions in the ferrite matrix. As pearlite is a eutectoid phase mixture, composed of alternate ferrite and cementite lamellae, three different scales have been distinguished for the ferrite-pearlite steel gear grades: the *microscale* where e.g. the pearlite is modeled by a repetition of ferrite/cementite bi-lamellas, *the mesoscale* of the ferrite-pearlite microstructure and the *macroscale* of the cutting process.

A two-stage homogenization scheme is adopted here, avoiding time consuming homogenization of a single RVE with a detailed description of all inclusions and a fine lamella description within each pearlite grain. This two-level scheme has been applied in the past with success to the derivation of anisotropic flow curves of a ferrite-pearlite pipeline steel [6]. Then, at the mesoscale, effective flow curves of the ferrite-pearlite microstructures are derived for each steel grade. From these curves, microstructure dependent strain hardening parameters of the JC model are determined by least-square fitting. Eventually, to evaluate and compare the machinability of both alloys, orthogonal FE cutting simulations with the identified JC model are performed in Abaqus by means of the Coupled Eulerian-Lagrangian (CEL) formulation.

2. Materials Characterization

The chemical composition of the investigated steel grades is given in Table 1. The Georgsmarienhütte provided the reference steel while the substitute steel was cast at the Institute for Ferrous Metallurgy (IEHK) of Aachen University.

Table 1. Chemical composition in wt % of the reference 18CrNiMo7-6 and of the substitute grade.

Steel	C	Cr	Ni	Mo	Mn	Nb	Al	Cu	Si
Ref.	0.18	1.55	1.6	0.27	0.5	0	0.31	0.30	0.24
Subst.	0.21	1.3	0	0.50	1.5	0.04	0.04	0.25	0.24

As expected, the Electron Probe Micro-Analyzes (EPMA) showed after the annealing step a ferrite-pearlite microstructure in both steel grades (see Fig. 1) in the bulk of the gear preforms. The lamellas of ferrite and cementite in the pearlite of the substitute grade are not so parallel and present some wrinkles; whereas the pearlite of the reference steel presents quasi-parallel lamellas.

EPMA images of the ferrite matrix show that small MnS inclusions exist in the 18CrNiMo7-6 alloy (see Fig. 2 a); whereas in the substitute steel small hard NbC carbides and few large CeS inclusions are detected in its ferrite matrix (Fig. 2 b and c). To identify the nature of the foreign phases in both ferrite matrices, the technique of Wavelength Dispersive X-ray Spectroscopy (WDS) was used, allowing the quantification of the chemical composition of the inclusions.

Using the image software AZtec, the number of inclusions, their shape and area are measured in microstructure windows of 1 mm^2 (see Table 2). The pearlite contents, given in Table 2, correspond to the local value at the same bulk location of both preforms. In the reference grade, 8495 MnS particles with an ellipsoidal shape are count (mean size: 0.132 μm^2). In the substitute steel 1474 small NbC carbides of ellipsoidal or prismatic shape having a mean size of 0.216 μm^2 and 198 large, quasi-spherical CeS inclusions with a mean size of 37.45 μm^2 are detected. The grain size of ferrite and pearlite is similar, so that their size is outlined together in Table 3 for both steel variants. Eventually, the lamella spacing and its extension are given also in Table 3. Compared to the 18CrNiMo7-6 steel, the substitute variant presents smaller grain sizes, a noticeable increase of pearlite content and a smaller interlamellar spacing, which induce a hardener flow behavior.

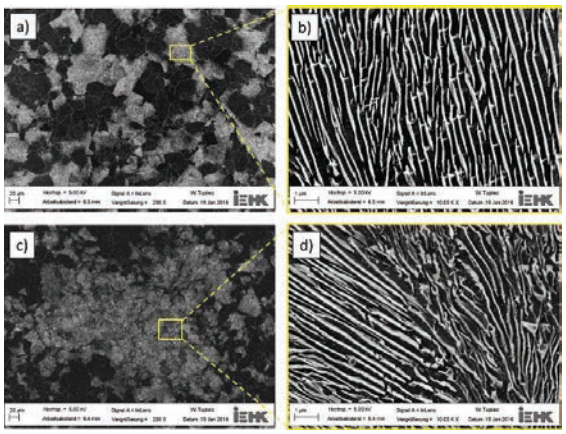

Fig. 1. EPMA analyses of the annealed 18CrNiMo7-6 steel a) and b) and of the substitute grade c) and d).

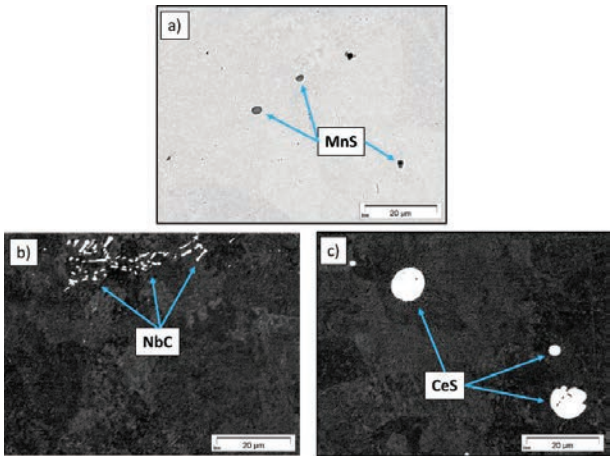

Fig. 2. EPMA image of the matrix of the reference steel a) and the annealed substitute grade b, c) showing detected inclusions.

Table 2. Phase content in wt % of both grades in the bulk of the gear preform.

Grade	Ferrite	Pearlite	Inclusions		
			MnS	NbC	CeS
Ref.	61	39	0.13	-	-
Subst.	51	49	-	0.021	0.322

Table 3. Average grain size, interlamellar spacing and length of the lamella in [μm] of both microstructures.

Grade	Grain size	Interlamellar spacing	Lamellar length
Ref.	29.0	0.3356	7.0
Subst.	17.2	0.2643	4.5

3. Experimental Setup of Compression Tests

To validate the flow curves determined by the RVE simulation, compression tests were performed on a servo-hydraulic press using cylindrical samples with a high of 9 mm and a diameter of 6 mm. They were manufactured from the forged and ferrite-perlite annealed gear wheel preform. The samples were compressed in a single hit using a strain rate of 2.5E-04 s^{-1} to a maximum strain of $\varepsilon \approx 0.75$. To reduce the influence of friction Teflon was used as lubricant. Subsequent, flow curves were determined from the measured force-displacement data. In this process, the elastic deformation as well as settlements in the machine were compensated. The resulting flow curves and the corresponding fitted strain hardening parameters of the classical Johnson-Cook model (Equation 1) are shown in Figure 3.

$$\sigma = \left(A + B\varepsilon^{n}\right)\left(1 + C\ln\frac{\dot{\varepsilon}}{\dot{\varepsilon}_0}\right)\left[1 - \left(\frac{T - T_r}{T_m - T_r}\right)^{m}\right] \quad (1)$$

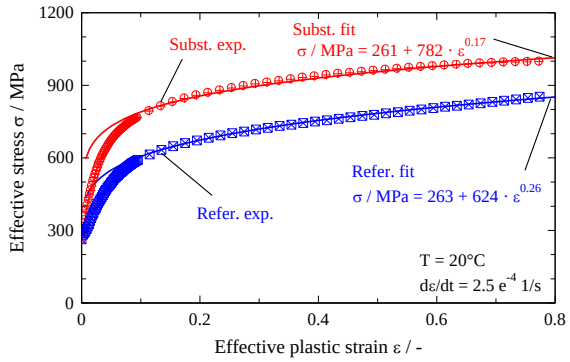

Fig. 3. Experimental quasi-static flow curves of both ferrite-pearlite steel grades derived from uniaxial compression tests.

As expected, the substitute grade presents stronger hardening than the reference alloy due to higher pearlite content and smaller mean grain size. Otherwise, plastic flow starts in the ferrite matrix of both steel grades at a low stress level (around 263 MPa) and is accompanied by a strong hardening before pearlite starts to yield. This effective elastoplastic behavior is typical for a dual-phase steel and constitutes a challenge for the least-square fit algorithm. Compared to the reference grade, the hardening coefficient B of the substitute steel increases by 25%; whereas the hardening exponent n decreases by -34.6% due less hardening increase at large strains.

4. Multiscale Modeling

The characterization of both steels reveals that the mean size of the MnS ($d = 0.132\ \mu m^2$) and NbC ($d = 0.216\ \mu m^2$) inclusions in the ferrite matrix of the reference or substitute steel is an order of magnitude smaller than the mean size of ferrite or pearlite grains: $d \geq 17\ \mu m^2$. On the other side, the grain size of the larger CeS inclusions is however of the same order of magnitude. Based on these observations, the two-level homogenization scheme, developed in [6], is generalized here. Indeed, at the microscale, not only the bi-lamella formed of ferrite and cementite layers is homogenized but also the reference ferrite matrix, containing MnS particles, and the substitute ferrite matrix, dotted with small NbC carbides, are homogenized separately. Moreover, at the mesoscale, the RVE of the substitute alloy contents not only effective pearlite grains randomly distributed in an effective ferrite matrix but also large CeS inclusions.

4.1. Homogenization of the pearlite bi-lamella

In order to perform the homogenization analysis by virtual testing, not only the design of the bi-lamella for both alloys but also the mechanical properties of the involved phase, namely ferrite and cementite, have to be specified firstly. As both steel grades are hypo-eutectoid steels, the orientation relationship between ferrite and cementite of Isaichev [7] is adopted here. Based on the respective chemical composition of both steel grades (see Table 1), the Gosh and Olson approach [8] is used to evaluate the cubic elastic constants of the ferrite phase at room temperature, as shown in Table 4.

Table 4. The cubic elastic constants of the ferrite phase at room temperature.

Grade	C11 / GPa	C12 / GPa	C44 / GPa
Ref.	227.6	131.3	115.1
Subst.	229.2	132.2	115.9

The isotropic work-hardening law of ferrite in pearlite is calculated according to the physically based micro-model of Gutierrez and Altuna [9]. The flow stress σ^Y is given there by:

$$\sigma^{Y} = \sigma_0 + \alpha M G b\sqrt{\frac{\left[1-\exp(-k_2 M\bar{\varepsilon}^{pl})\right]}{bLk_2}} + \rho_0 \exp\left(-k_2 M\bar{\varepsilon}^{pl}\right) \quad (2)$$

With α equals to 0.33, M the Taylor factor, b the norm of the Burgers vector, G the shear modulus, L the dislocation mean free path, k_2 the dislocation annihilation constant, ρ_0 the initial dislocation density and σ_0 an intrinsic stress, which is related to the chemical composition of the alloy by:

$$\sigma_0 = 77 + 32Mn + 678P + 83Si + 39Cu - 31Cr + 11Mo + 5544C_{SS} \quad (3)$$

In this expression the concentrations are expressed in wt.% and C_{SS} is the carbon solution in ferrite. As multiplied by a large factor, its value is the dominant term, which is difficult to determine as the initial annealed state is not in thermodynamic equilibrium. We adopt here $C_{SS} = 0.0193\%$ for the reference steel and $C_{SS} = 0.0209\%$ for the substitute respectively. Moreover, the unknown residual dislocation density is set to

$\rho_0 = 1.\ 10^{14}\ m^{-2}$ for both alloys; whereas the dislocation mean free path L is set to the extension of the ferrite layer in the bi-lamella RVE: 7 µm for the reference grade and to 4.5 µm for the substitute, as some wrinkles are observed in Fig. 1.

On the other hand, cementite is known to be substantially harder than ferrite and quite brittle. It has an orthorhombic lattice, for which Jiang et al. [10] performed first principle calculation in order to derive its single crystal elastic coefficients, reported also in [6]. Cementite presents a strong elastic anisotropy with a very law shear stiffness C_{44}. As cementite is metastable at all temperatures, it is difficult to produce a test specimen for mechanical testing. Laschet et al. [6] have shown that it is important to take non only its inelastic behavior but also the anisotropy of this behavior into account, by adopting a mean yield stress of 4 GPa and the yield stress ratios (R_{XX} = 1, R_{YY} = 0.89, R_{ZZ} = 0.83, R_{XY} = 0.18, $R_{XZ} = R_{YZ}$ = 0.7). The thickness of the bi-lamella RVE design of each steel grade corresponds respectively to the measured interlamellar spacing (see Table 3). Assuming thermodynamic equilibrium of pearlite eutectoid, the volume fractions of cementite and ferrite are V_C = 1/9 and V_F = 8/9 respectively. More delicate is the definition of the length and width of the microscale RVE's. Here the measured mean length of pearlite lamellas is adopted for the RVE length and width: $l_{Ref} = w_{Ref}$ = 7 µm and $l_{Subst} = w_{Subst}$ = 4.5 µm. These simple RVE's are enmeshed by 7200 linear hexahedral elements and periodic boundary conditions are applied in its thickness direction.

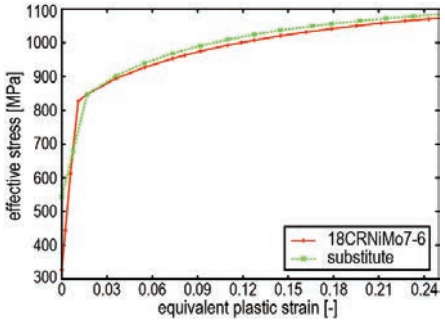

Fig. 4. Effective tensile elasto-plastic stress-strain curves of pearlite.

In Fig. 4 the predicted elasto-plastic flow curves of both alloys are drawn for a uniaxial tensile test in the thickness direction of the bi-lamella. Independent of the pearlite design, the flow curves present a strong change in hardening when cementite begin also to yield. In fact, initial yielding happens only in the ferrite layer; whereas cementite continues to deform elastically. Compared to 18CrNiMo7-6 grade, the substitute variant has a higher initial yield stress and hardening. Note that before cementite yields, slightly larger plastic deformation is observed also in the ferrite layer.

4.2. Effective ferrite matrix of the 18CrNiMo7-6 steel

The MnS inclusions have a weaker elasto-plastic behavior as the ferrite phase. Their initial yield stress σ^Y is 88.2 MPa and at $\bar{\varepsilon}^{pl}$ = 0.2, the equivalent stress reaches 130 MPa. The elasto-plastic constitutive law is expressed again via the Guttierez-Altuna micro-model. The main difference to the ferrite layer in pearlite is the mean free path L, which is taken to be equal to the main grain size (29 µm). At the microscale, a small RVE of 80 μm^3 extension is generated with the commercial program Digimat-FE [11]. 3D periodic boundary conditions are imposed on the outer RVE surface. 28 small MnS spheres, having a volume fraction of 0.03875%, and 15 MnS ellipsoids (V_f = 0.09225%) are distributed randomly within the ferrite matrix. Uniaxial virtual tensile test has been performed on the discretized RVE. To quantify the stiffness and hardening reduction of the effective ferrite matrix, the Ludwik coefficients A, B and n (see 1st term of eq. 1) are derived by least-square fit (Ferrite: A = 322.9 MPa, B = 385.2 MPa, n = 0.4273; Ferrite+MnS: A = 308.5 MPa, B = 392.8 MPa, n = 0.4230). Mainly the initial yield stress A is affected by the presence of MnS inclusions.

4.3. Effective ferrite matrix of the substitute steel

The NbC carbides are stiff inclusions in the ferrite matrix of the substitute grade. They are cubic and deform only elastically: C_{11} = 557.3 GPa ; C_{12} = 162.4 GPa ; C_{44} = 146.5 GPa; but present a noticeable Zener anisotropy: $A^z = \frac{2C_{44}}{(C_{11}-C_{12})} = 0.74$.

Equation (2) describes again the mechanical behaviour of the ferrite matrix, which is harder in the substitute alloy do to the smaller grain size: 17.16 µm instead 29 µm. A periodic RVE of extension 100 μm^3 is generated containing 9 randomly distributed ellipsoids of aspect ratio a = 1.3, having a total V_f = 0.0105%, and 4 prism inclusions with V_f = 0.0109%. Again a virtual tensile test is achieved leading to following fitted hardening parameters for the effective matrix: A = 300.5 MPa; B = 517.9 MPa and n = 0.46; whereas for the pure ferrite matrix we have: A = 299 MPa; B = 479.5 MPa and n = 0.4273. Nevertheless, the volume content of NbC carbides (V_{NbC} = 0.02133%) is small, the effective hardening increases noticeably: ΔB = 8% and Δn = 7.6%.

4.4. Mesoscale homogenization of both steel grades

According to its pearlite content of 39% (see Table 2), an RVE of extension 250 μm^3 (see Fig. 5 a) is built by applying successively Digimat-FE for the random seek of prismatic pearlite grains within the RVE and Abaqus CAE for the coarse mesh generation (237,585 elements). To achieve *quasi-isotropic grain orientation distribution*, the pearlite grains are divided in 40 groups, each group corresponds to a specific Pilvin grain orientation [12]. Due to its higher pearlite content (V_{pearl} = 48.65%) the generation of an RVE with Digimat-FE becomes delicate for the substitute grade as the grain size of the last groups are reduced strongly by trying to achieve the desired volume content. Eventually, a small RVE of extension 125 μm^3 and discretized by a fine mesh (863,545 elements) is generated (see Fig. 5.b). This RVE contains three CeS inclusions (V_{CeS} = 0.3217%.), which deform elastically. Uniaxial virtual compression tests are performed for both steel grades on their respective periodic RVE. In Figure 6, the predicted effective flow curves of both steel grades are drawn. For each steel grade, the corresponding fitted quasi-static JC parameters are given also in this figure.

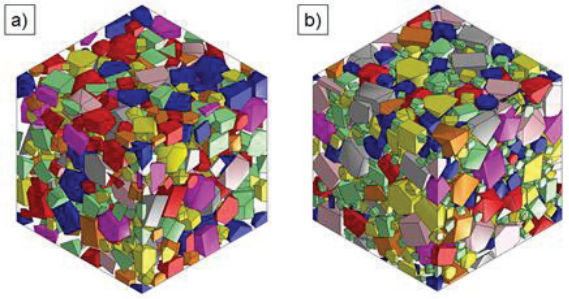

Fig. 5. Generated RVE's a) Reference; b) Substitutive steel.

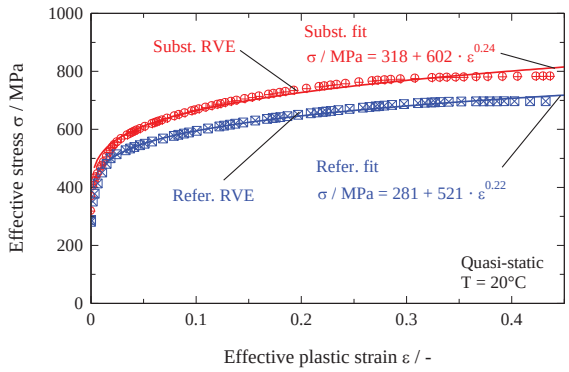

Fig. 6. Predicted effective flow curves of reference and substitute steel.

Independent of the considered steel grade, both predicted flow curves present a strong change in their hardening behavior, when the effective pearlite grains begin also to yield. Due to its higher pearlite content and the smaller grain size (17.2 µm vs. 29.0 µm), the substitute alloy presents a stiffer equivalent hardening behavior, characterized by an increase of all quasi-static JC parameters: ΔA = 13.2%; ΔB = 15.5% and Δn = 9.1%. Both fitted JC parameter sets are transferred then to the macroscale cutting simulation model.

5. Cutting validation tests for the material law

To validate the developed microstructure-based material model, experimental and simulative orthogonal cutting tests are carried out on both investigated steel grades. A cutting speed of v_c = 100 m/min, an undeformed chip thickness h = 0.20 mm and width of cut b = 3.0 mm are adopted there as well as a coated cemented cut-off insert (Sandvik 4225, multilayer Al_2O_3+TiN, rake angle: γ_n = 6°, clearance angle: α = 3°, cutting edge radius $r_ß$ = 60 µm). The cutting experiments are performed dry on an advanced fundamental test-bench based on a vertical broaching machine tool (max. cutting speed: 150 m/min, max. force: 80 kN, max. power: 40 kW), see Fig. 7 a). The cutting tool is mounted on a three-component piezoelectric dynamometer in order to measure the cutting force. Because of the fixed tool, the chip formation process can be recorded by means of a high speed camera of type Vision Research Phantom v7.3 (frame rate: 500,000 fps at 32 x 16 pixels).

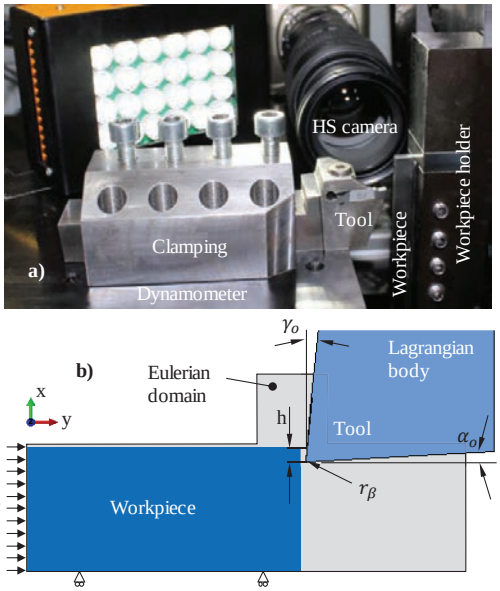

Fig. 7. a) Experimental setup; b) CEL computation FE model.

The FE cutting simulations are conducted by means of a thermo-mechanically coupled model using the coupled Eulerian-Lagrangian (CEL) formulation in the Explicit FE code Abaqus (see Fig. 7 b). In this CEL model, the tool is fixed in space and described by the Lagrangian formulation. The chip formation is simulated by the continuous flow of the work material through the Eulerian mesh against the tool. Due to the absence of mesh deformation in the workpiece, no remeshing is needed and large plastic deformation can be realized. The thermo-mechanical material flow behavior in the simulation is described with the JC material law according to Eq. 1. The parameters A, B and n of Eq. 1 are determined for both steels in section 3 and 4. The strain rate dependent JC parameters, C and m, are taken from the literature [13]. To simulate chip segmentation during orthogonal cutting the substitute steel, the JC ductile damage model [14] is used:

$$\varepsilon_f = [D_1 + D_2 \exp(D_3\, \sigma^*)] \cdot (1 + D_4 \ln \dot{\varepsilon}^*) \cdot (1 + D_5\, T^*) \quad (4)$$

Table 5 summarizes the material law parameters used in the cutting simulation.

Table 5. The JC material law and damage parameters for both steel grades.

Steel	**A**	**B**	**n**	**C**	**m**
Refer. exp.	263	624	0.26	0.017	1.3
Refer. RVE	281	521	0.22	0.017	1.3
Subst. exp.	261	782	0.17	0.016	1.25
Subst. RVE	318	602	0.24	0.016	1.25
Steel	**D_1**	**D_2**	**D_3**	**D_4**	**D_5**
Subst. exp./ RVE	0.05	0.8	-1.54	0.01	1

The tool is modeled as rigid body and has a constant mesh to calculate the temperature distribution within the tool. The cutting material data used in the simulation was obtained from the literature [15]. Friction between the tool and work material is described by the proportional friction model with a friction coefficient of µ = 0.2 (empirical value taking coating and higher contact temperature into account, [15]). For the thermal

boundary conditions, conduction and convection of the generated heat are applied. The gap conductance and the thermal convection coefficient between two contacting surfaces are assumed to be equal to 10^7 W/m^2 °C and 20 W/m^2 °C, respectively [16].

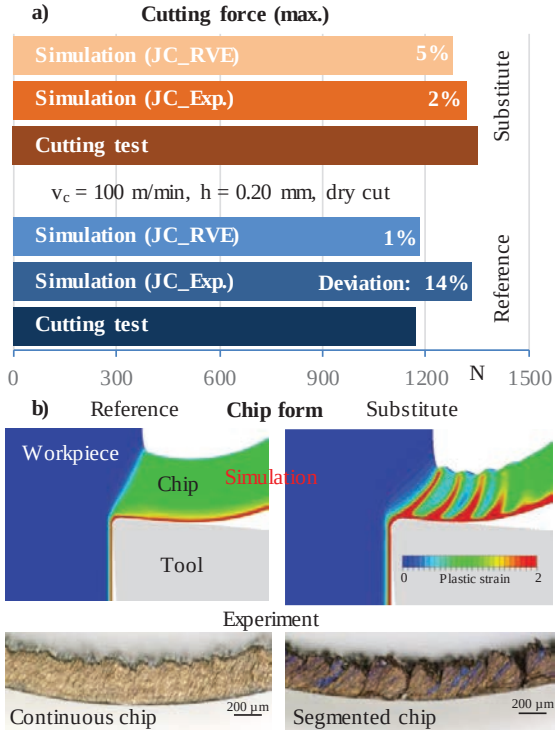

Fig. 8. Model validation: a) cutting force, b) chip form.

Fig. 8 shows a comparison between the experimental and FE predicted cutting force and the chip form for two different JC material laws. The first one is derived from compression tests and the second from the RVE concept. Regarding the cutting force, a better prediction (max. deviation 5%) could be obtained with the RVE approach compared to the other one (max. deviation 14%, as shown in Fig. 8 a). When cutting the investigated steel grades, continuous chip form could be detected by the 18CrNiMo7-6 grade, but segmented chips for the substitute variant (see Fig. 8 b).

6. Conclusions

In this research work, a multiscale constitutive material model is developed and successfully validated by means of CEL simulation of orthogonal cutting two different steel grades. The developed material model is based on the RVE concept and describes the onset of yielding and the strain hardening of ferritic-pearlitic steels proceeding from the material microstructure. The main results achieved in this investigation can be summarized as follows:

- The developed multiscale model directly links the mechanical material properties to the microstructure.
- A two-stage homogenization scheme is adopted to avoid time consuming homogenization of a single RVE with a detailed description of all inclusions and a fine lamella description within each pearlite grain.
- The cutting simulation results are close to the cutting tests when using the material law derived from the respective RVE model.

In future, to still improve the RVE model predictions, an inverse method will be applied in order to tackle some unknown micromechanical model parameters (ρ_0, C_{SS}, etc.).

Acknowledgements

The authors would like to thank the German Research Foundation (DFG) for the funding support provided to develop the present work in the project Cluster of Excellence “Integrative Production Technology for High-Wage Countries”.

References

[1] Konovalov S, Prahl U. Tailoring the microstructure for micro-alloyed carburizing steels by an ICME approach. Fundamentals and Applications of Mo and Nb Alloying in High Performance Steels; H. Mohrbacher, Editor 2015; 2:215-225.
[2] Schmitz J, Prahl U. Integrative Computational Materials Engineering - Concepts and Applications of a Modular Simulation Platform. Wiley VCH 2012; Germany.
[3] Johnson GR, Cook WH. A consitutive model and data for metals subjected to large strain, high strain rates and high temperatures. Proc. of the 7th Int. Symposium on Ballistics 1983; Hague, Netherlands.
[4] Daridon L, Oussouaddi O, Ahzi S. Influence of material constitutive models on the adiabatic shear band spacing: MTS, power law and Johnson-Cook models. Int. Jnl. of Solids and Struct. 2004; 41:3109-3124.
[5] Spirdione J, Visser W, Maciejewski K, Ghonem H. Role of pearlite colonies on the dynamic flow stress of low carbon steel. Mat. Scien. & Engng A 2017; 629:446-454.
[6] Laschet G, Fayek P, Henke T, Quade H, Prahl U. Derivation of anisotropic flow curves of ferrite-pearlite pipeline steel via a two-level homogenization scheme. Mat. Scien. & Engng A 2013; 566:143-156.
[7] Isaichev IV, Tekh Zh. Fiz. 1947; 47:835-838.
[8] Gosh G, Olson GB. The isotropic shear modulus of multicomponent Fe-base solid solutions. Act. Mater. 2002; 50:2655-2675.
[9] Gutierrez I, Altuna MA. Work-hardening of ferrite and microstructure-based modelling of its mechanical behavior under tension. Act. Mater. 2008; 56:4682-4690.
[10] Jiang C, Srinivasan SG, Caro A, Maloy SA. Structural, elastic and electronic properties of Fe_3C from first principles. J. of Appl. Phys. 2008; 103, 043502:1-8.
[11] DIGIMAT software, version 5.1, Louvain-la-Neuve 2014; Belgium.
[12] Pilvin P, Cailletaud G. Proc. IUTAM Creep in Structures IV 1990, Cracow.
[13] Abouridouane M, Klocke F, Lung D, Adams O. A new 3D multiphase FE model for micro cutting ferritic-pearlitic carbon steels. CIRP Annals - Manufacturing Technology 2012; 61:71-74.
[14] Johnson GR, Cook WH. Fracture characteristics of three metals subjected to various strains, strain rates, temperatures and pressures. Engineering Fracture Mechanics 1985; 21(1):31-48.
[15] Puls H, Klocke F, Lung D. Experimental investigation on friction under metal cutting conditions. In Wear 2014; Jg. 310:63-71.
[16] Abouridouane M, Klocke F, Lung D, Veselovac D. The mechanics of cutting: in-situ measurement and modelling. Procedia CIRP 2015; 31:246-251.